21st Australasian Fluid Mechanics Conference
Adelaide, Australia
10-13 December 2018

Heat transport in two-phase vertical natural convection using an Euler–Lagrange approach

C. S. Ng[1], V. Spandan[1], D. Lohse[1] and R. Verzicco[1,2]

[1]Physics of Fluids Group, Max Planck Center for Complex Fluid Dynamics, J. M. Burgers Center for Fluid Dynamics and MESA+ Research Institute, Department of Science and Technology, University of Twente, P.O. Box 217, 7500 AE Enschede, The Netherlands

[2]Department of Mechanical Engineering, University of Rome 'Tor Vergata', Italy

Abstract

We present numerical results of dispersed droplets in vertical natural convection (VNC) flow, which is a buoyancy driven flow between differentially heated vertical walls. Our focus is to study the effects of droplets on the local statistics of heat transport in natural convection, where heat transport enhancement due to bubbles has recently been reported [5]. Our numerical simulations are fully-resolved and based on an Euler–Lagrange approach with two phases: the first is the carrier phase (liquid), which is solved by a second-order accurate finite-difference scheme and marched in time using a fractional-step approach; the second is the dispersed phase (droplets) that are much larger than the Kolmogorov length scale. The interfacial droplet boundaries and deformations are modelled by an immersed boundary method and an interaction potential approach, respectively. We show that the heat flux is slightly enhanced for the Rayleigh number range 1.3×10^8–2.3×10^9 and Prandtl number of 7, which can be attributed to droplet induced mixing.

Introduction

The motions of bubble columns agitate the surrounding liquid and can give rise to enhanced heat and momentum transport. This phenomenon is important for various engineering applications, for example in stirred tank reactors [4], water treatment plants, steel industry [6] and mechanical flotation cells [10]. In this study, we focus on the influence of bubble columns on the heat transport within a liquid. Our model setup is the VNC flow (figure 1*a*), similar to [11, 8, 9]. The bubbles are idealised as light droplets and are allowed to freely rise within the domain (figure 1*b*). The underlying mechanism of interest is droplet induced mixing, generally assumed to be controlled by (*i*) the capture and transport by droplet/bubble wake, and (*ii*) dispersion by droplet/bubble-induced turbulence [1].

Since we are interested in large droplets, i.e. droplet diameter larger than the Kolmogorov length scales, fully-resolved simulations are necessary in order to account for the inhomogeneous hydrodynamic forces acting at the droplet interface. To achieve this, we perform direct numerical simulations (DNS) coupled with the immersed boundary method (IBM) and interaction potential approach, which are versatile numerical methodologies to simulate fully-coupled fluid flows with deformable interfaces, e.g. [13, 7]. IBM offers some computational advantages over existing numerical methods for multiphase flows (e.g. volume-of-fluid, level-set and front tracking). For instance, in IBM, the underlying discretised grid is fixed and no sharp interfaces need to be resolved [12]; this method therefore allows simulations of multiphase flows to be easily scaled-up.

Flow Setup

The setup for single-phase VNC is a buoyancy driven flow confined in a cell (see figure 1*a*), with hot and cold vertical walls (at $z/L_z=0$ and 1) and also adiabatic horizontal walls (at $x/L_z=0$ and 2.4). The flow is governed by the continuity equation,

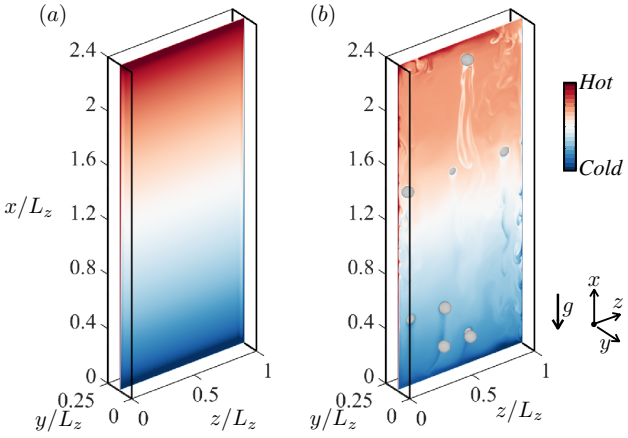

Figure 1: Schematic of vertical natural convection (VNC) in a cell, visualising the temperature field: (*a*) single-phase VNC, and (*b*) two-phase VNC. The hot and cold walls are at $z/L_z=0$ and 1, respectively. g is the direction of gravity.

$\partial_i u_i=0$, and the momentum and temperature equations are respectively given by,

$$\partial_t u_i + u_j\partial_j u_i = -\frac{1}{\rho_{ref}}\partial_i p + \delta_{i1}g\beta(\theta-\theta_{ref}) + \nu\partial_j^2 u_i + f_i, \quad (1)$$

$$\partial_t\theta + u_j\partial_j\theta = \kappa\partial_j^2\theta, \quad (2)$$

where $\partial_t\equiv\partial/\partial t$, $\partial_i\equiv\partial/\partial x_i$, $(i,j=1,2,3)$ and repeated indices imply summation. We define θ_{ref} as the reference temperature, β as the thermal expansion coefficient of the fluid, ν as the kinematic viscosity and κ as the thermal diffusivity, all assumed to be independent of temperature. The aspect ratio of the setup $\Gamma=L_x/L_z$ is chosen to be 2.4, which models the dimensions of the water column experiment performed by [5]. No-slip and no-penetration boundary conditions are imposed on the velocity at all walls. Periodic boundary conditions are imposed on u_i, p and θ in the y-direction. The Rayleigh, Nusselt and Prandtl numbers are respectively defined as

$$Ra\equiv g\beta\Delta L_z^3/(\nu\kappa), \quad Nu\equiv f_w L_z/(\Delta\kappa), \quad Pr\equiv\nu/\kappa, \quad (3)$$

where, $\Delta\equiv T_h-T_c$ is the temperature difference between the vertical walls, $f_w\equiv\kappa|d\overline{\theta}/dz|_w$ is the wall heat flux and $(\cdot)|_w$ denotes the wall value. For all simulations, we set the Pr value equal to 7, corresponding to water. For confined thermal convection problems, the aspect ratio Γ is also an additional parameter (see for example in [15]), however, in this study we restrict our analysis to the Rayleigh number defined based on L_z and for a fixed Γ value. In equation (1), f_i is a time-dependent source term resulting from the immersed boundaries, which imposes back-reaction forces from the dispersed droplets phase onto the liquid carrier phase.

In this study, we consider droplets that are one order of magnitude larger than the Kolmogorov length scale $\eta \equiv (\nu^3/\langle\varepsilon\rangle)^{1/4}$, where $\langle\varepsilon\rangle \equiv \nu\langle(\partial u_i/\partial x_j)^2\rangle$ is the volume-averaged kinetic energy dissipation rate and $\langle\cdot\rangle$ denotes volume-averaged quantities, and so, the hydrodynamic forces acting on the droplet are inhomogeneous along the droplet interface and need to be fully resolved. To accomplish this, the droplet interface is discretised as an unstructured mesh that is composed of triangular elements [12, 3], which are dynamically linked as a spring-mesh system with the aim of minimising the total potential energy of the mesh. This approach is referred to as the interaction potential approach. Then, the external (hydrodynamic) forces from the fluid and internal forces from the mesh are calculated based on the centroid of the triangular elements, i.e. the Lagrangian markers. For additional details of the interaction potential approach, we refer the reader to [12]. The relevant interaction potential parameters used in this study are reported in the next section.

Numerical Details

The liquid phase is solved using direct numerical simulations (DNS) by a second-order accurate finite-difference scheme and marched in time using a fractional-step approach [14]. The streamwise, spanwise and wall-normal domain sizes are $L_x = 9.6L_y = 2.4Lz$, whereas $Ra = 1.3\times10^8$-2.3×10^9. The grid spacing is equal in the x- and y-directions, and is stretched using a clipped-Chebychev-type clustering in the z-direction in order to resolve the steep near-wall gradients at the hot and cold walls. The resolutions are selected such that $\max[\Delta x_i/\delta_\nu] \lesssim 3.3$ (see table 1), where Δx_i are the grid spacings in each ith direction and $\delta_\nu \equiv \nu/u_\tau$ is the viscous length scale which is based on the shear velocity scale $u_\tau \equiv (\nu|\mathrm{d}\overline{u}/\mathrm{d}z|_w)^{1/2}$. Here, $\overline{(\cdot)}$ denotes xy-plane-averaged statistics.

For the dispersed phase, the volume fraction, $\alpha = 5\times10^{-3}$. The deformability of the droplets is set by the Weber number, $We \equiv \rho U_\Delta^2 d/\sigma$, which measures the inertia forces relative to surface tension forces, where ρ is the density of the liquid phase, $U_\Delta \equiv (g\beta\Delta L_z)^{1/2}$ is the free-fall velocity, d is the droplet diameter and σ is the surface tension. Because σ is an additional input parameter for our study, it is prescribed by tuning the constants of the phenomenological spring-mesh system described in the previous section. According to the selection criteria described in [12], we select the following dimensionless spring constants: the in-plane elastic constant $k_e^* = 0.03$, the bending constant, $k_b^* = k_e^*/60$, volume constant $k_v^* \approx 3\times10^3 k_e^*$ and area constant $k_a^* = k_e^*$. For this study, $We \approx 3\times10^{-2}$, corresponding to a relatively stiff droplet. In addition, we set the density ratio of the droplet relative to the fluid, $\hat{\rho} \equiv \rho_d/\rho = 0.99$.

The simulations are split into two stages. First, the single-phase simulations are run for at least 200 dimensionless turnover times, where a turnover time is defined by the free-fall period, L_z/U_Δ, so that a statistically stationary state is first achieved. Then, the droplets are placed randomly inside the domain, where each droplet is initiated with a vertical velocity component that corresponds to its respective height thus mimicking the velocity distribution of rising bubbles in a water column. Upon reaching 2 grid points from the top boundary, the droplets are removed and placed randomly at the bottom of the domain–this approach guarantees a constant volume fraction throughout our simulations. The statistics are sampled for at least 100 dimensionless turnover times (the first 100 dimensionless turnover times are discarded).

Presently, we restrict our simulations to droplets with interfaces that are surfactant-contaminated (no-slip) and thermally passive (no temperature boundary condition) as these conditions can be handled easily from a numerical point-of-view. But, even with these simplified boundary conditions, we emphasise that the simulations are still two-way coupled. The diameter of the droplet $d = 0.08L_z$ and the number of grid points for the Eulerian grid are chosen such that the droplet diameter is at least 20 times larger than the Eulerian grid spacings, which occurs in the bulk of the cell due to grid stretching. Thus, the same resolutions ($n_x\times n_y\times n_z = 960\times96\times384$) are employed for the two-phase simulations. Since d is kept constant, $d/\eta \approx 8$ for the lowest Ra and and ≈ 19 for the highest Ra in our study. In addition, the values of the Reynolds number of the droplet, $Re_d \equiv (u_d - \langle u\rangle)d/\nu$ lie in the ranges $\approx$15 to 70 for the lowest Ra and $\approx$70 to 300 for the highest Ra, where u_d is the vertical velocity of the droplet ($\langle u\rangle$ is zero, statistically). Note that the current Re_d values are much lower than in physical experiments (e.g. $Re_d \approx 600$ as in [5]). For all simulations with a dispersed phase, each droplet is discretised using 5120 Lagrangian markers. The simulation parameters for this study are summarised in table 1.

Ra ($\times10^8$)	α ($\times10^{-3}$)	Δx^+	Δy^+	Δz^+_{min}	Δz^+_{max}	$T_s U_\Delta/L_z$
1.3	-	1.1	1.1	0.17	1.6	202
2.3	-	1.4	1.3	0.21	2.0	289
4.1	-	1.7	1.6	0.26	2.5	400
7.2	-	2.1	2.0	0.32	3.1	400
13.0	-	1.8	1.7	0.19	2.6	300
23.0	-	2.2	2.1	0.23	3.3	200
1.3	5.0	0.7	0.7	0.08	1.1	240
2.3	5.0	0.9	0.9	0.10	1.4	240
4.1	5.0	1.1	1.1	0.12	1.7	228
7.2	5.0	1.4	1.4	0.15	2.1	220
13.0	5.0	1.7	1.7	0.19	2.6	127
23.0	5.0	2.1	2.1	0.23	3.2	148

Table 1: Simulation parameters of the present DNS cases. The number of grid points are $n_x\times n_y\times n_z = 960\times96\times384$ for all cases, except for $Ra \leqslant 7.2\times10^8$ for the single phase cases, where $n_x\times n_y\times n_z = 640\times64\times256$. T_s is the simulation sampling time.

Influence of Buoyant Droplets on Mean Statistics

To establish a reference, the single phase mean temperature profiles $(\overline{\theta} - \theta_{ref})/\Delta$ and single phase mean vertical velocity profiles $\overline{u}/U_\Delta$ are shown in figure 2. Similar to VNC in a doubly-periodic channel [8], the mean profiles of the single phase case are statistically antisymmetric about the xy-plane at $z = 0.5L_z$. However, when VNC is confined in a cell, $\overline{u}|_{z/L_z=0.5}$ is statistically zero with no persistent shear. In the cell centre, the vertical velocity is stabilised by a vertical temperature gradient, as can be seen in the visualisation in figure 1*a*.

With $\alpha = 5\times10^{-3}$, we observe subtle changes in the mean velocity and temperature profiles (see dashed lines in figure 2). The maxima and minima of the near-wall mean velocities are farther from the walls at lower Ra and some distortion of the mean profiles can also be observed, which is consistent with the distortions in the two-phase mean temperature profiles reported in [5]. In particular, we observe some attenuation of the near-wall overshoots (deviations from the mean bulk velocity and mean bulk temperature, e.g. at $z/L_z \approx 0.04$ in figure 2*a*), suggesting that mixing mechanisms in VNC are important even with the introduction of light drops.

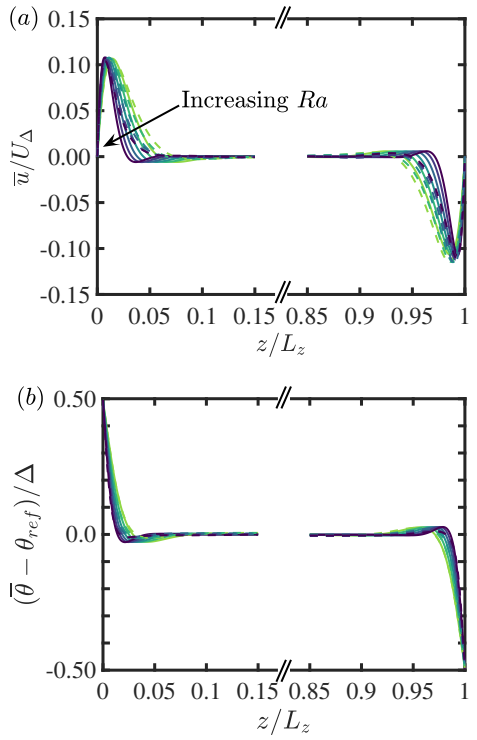

Figure 2: (*a*) Profiles of mean vertical velocity for pure VNC (solid lines) and multiphase VNC (dashed lines). (*b*) Profiles for mean temperature. Note that because the bulk region is statistically zero, only near-wall statistics are shown, i.e. $0 \leqslant z/L_z \leqslant 0.15$ and $0.85 \leqslant z/L_z \leqslant 1$. The influence of the two-phase VNC is subtle.

When $\alpha = 5 \times 10^{-3}$, the near-wall temperature gradients become steeper at higher *Ra* values. These trends are not easily seen in figure 2*b*, but we can inspect the trends by plotting the compensated values of *Nu*, as shown in figure 3. Note that since the droplets are thermally passive in our simulations, it can be shown that $(\mathrm{d}\overline{\theta}/\mathrm{d}z)|_{z/L_z=0} = (\mathrm{d}\overline{\theta}/\mathrm{d}z)|_{z/L_z=1} = \text{const.}$ by integrating equation (2) over the domain. Therefore, we compute *Nu* for the droplets-laden VNC by averaging the temperature gradients at the hot and cold walls, in accordance with equation (3). The values of *Nu* is comparable at lowest *Ra* but with increasing *Ra*, *Nu* increases by up to 10% relative to the single-phase *Nu*. For comparison, the *Nu* values for the single phase experiments of [5] are also plotted in figure 3; these experimental values are much higher than the single phase results of the present study because the liquid in the experiments has a free surface.

Although we observe an enhancement in *Nu*, the relative increase is less prominent compared to experiments (for example, [5] reported approximately one order of magnitude increase in *Nu*). To explain this difference, we define the droplet Froude number

$$Fr^2 \equiv \frac{U_\Delta^2}{gL_z\alpha/(\hat{\rho})} = \frac{Ra}{Ra_d} \tag{4}$$

where $Ra_d \equiv \alpha g L_z^3/(\nu\kappa\hat{\rho})$ is the droplet Rayleigh number, which is inspired by the analogy with thermal convection (see for example in [2]). The Froude number characterises the relative strength of thermal driving to the driving of the flow by the rising droplets. In the experiments of [5], $Fr^2 \approx 1.5 \times 10^{-6}$, whereas in our simulations $Fr^2 = 100$. Evidently, the present simulations are dominated by thermal buoyancy and the flow is in a different regime than the experiments of [5].

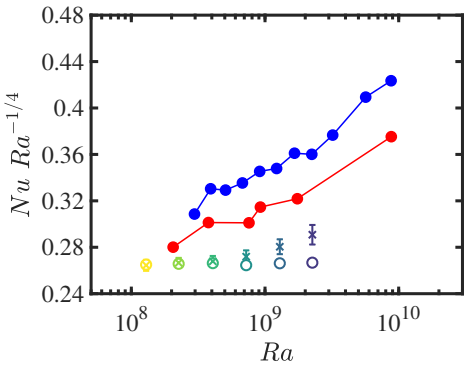

Figure 3: Plot of compensated *Nu* versus *Ra* for the pure VNC case (open circles) and dispersed VNC case (crosses). With buoyant droplets, the VNC flow exhibit an increase in *Nu* at higher *Ra*, but still lower than the *Nu* trends of pure VNC with free-slip boundary conditions, as shown by the experimental and DNS data from [5] (solid blue and solid red symbols, respectively).

Influence of Buoyant Droplets on Turbulent Statistics

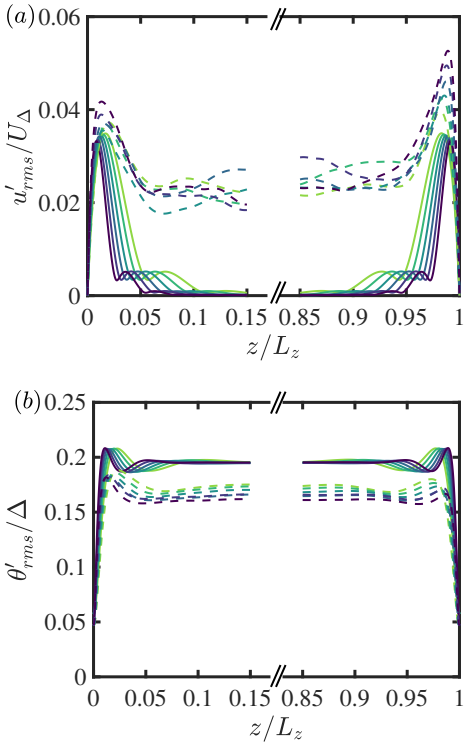

Figure 4: Similar plots as in figure 2, but now for (*a*) root-mean-square of vertical velocity fluctuations $u'_{rms} \equiv (\overline{u'u'})^{1/2}$, and (*b*) root-mean-square of temperature fluctuations $\theta'_{rms} \equiv (\overline{\theta'\theta'})^{1/2}$. The two-phase flow has a more pronounced effect on the turbulent statistics: in (*a*) vertical velocity fluctuations are increased due to larger intensity of vertical liquid fluctuations [1], in (*b*) temperature fluctuations are lower due to capture and transport of colder fluid in the droplets' wakes.

Moving on to the influence on the fluctuating quantities, in figure 4*a* we find that the root-mean-square (r.m.s.) of the vertical velocity fluctuations, $u'_{rms} \equiv (\overline{u'u'})^{1/2}$, are increased not only in the near-wall regions but also in the bulk of the flow. The magnitudes of the maxima close to the colder wall are between 6%–26% higher than the maxima close to the hotter wall. A

straightforward explanation of the higher magnitudes near the colder wall is that velocity fluctuations are increased due to the rising drops that oppose the downwards mean flow. In figure 4*b*, the profiles of temperature r.m.s. are lower than the single phase results. This can be explained by the capture and transport of the colder fluid at the bottom of the cell by the droplet wakes, as can be observed in figure 1*b*.

Droplet Distribution

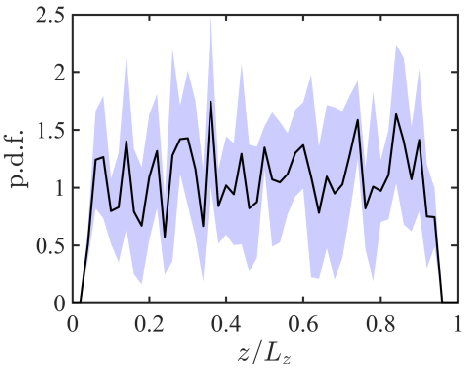

Figure 5: Normalised p.d.f. of droplets distribution as a function of wall-normal location, averaged over all *Ra* cases. The light blue shade shows the standard deviation of the p.d.f. at the respective z-location.

In figure 5, we quantify the distribution of the droplets as a function of wall-normal location z using a normalised probability density function (p.d.f.), which is averaged in x- and y-directions as well as in time. The distribution is roughly close to uniform throughout the domain, implying a relatively homogeneous distribution of droplets throughout the simulation domain and presumably a uniform contribution to the vertical velocities in the bulk flow, as seen in figure 4*a*.

Conclusions

Using light droplets, we investigated the influence of mixing on the heat flux in two-phase VNC for a range of Rayleigh numbers from 1.3×10^8 to 2.3×10^9 and Prandtl number of 7. Since the droplets are larger than the Kolmogorov scales, we perform fully resolved direct numerical simulations using the IBM coupled with the interaction potential approach.

The motion of the rising droplets distort the near-wall mean statistics, and the influence becomes more pronounced at higher values of *Ra*, as highlighted by the increasing *Nu* values. The vertical velocity fluctuations are also increased compared to the single-phase case. This increase is especially prominent in the bulk region of the flow, which is linked to the homogeneous distribution of droplets. Collectively, we show that the presence of light droplets with a small droplet Rayleigh number (as compared to experiments) can contribute to mixing and enhanced heat transport in VNC.

Acknowledgements

This work is part of the research programme of the Foundation for Fundamental Research on Matter with project number 16DDS001, which is financially supported by the Netherlands Organisation for Scientific Research (NWO). The simulations were carried out on the national e-infrastructure of SURFsara, a subsidiary of SURF cooperation, the collaborative ICT organization for Dutch education and research. We also acknowledge PRACE for awarding us access to MareNostrum based in Italy at the Barcelona Supercomputing Center (BSC) under PRACE project number 2017174146.

References

[1] Alméras, E., Risso, F., Roig, V., Cazin, S., Plais, C. and Augier, F., Mixing by bubble-induced turbulence, *J. Fluid Mech.*, **776**, 2015, 458–474.

[2] Climent, E. and Magnaudet, J., Large-scale simulations of bubble-induced convection in a liquid layer, *Phys. Rev. Lett.*, **82**, 1999, 4827.

[3] de Tullio, M. D. and Pascazio, G., A moving-least-squares immersed boundary method for simulating the fluid–structure interaction of elastic bodies with arbitrary thickness, *J. Comput. Phys.*, **325**, 2016, 201–225.

[4] Deckwer, W.-D., On the mechanism of heat transfer in bubble column reactors, *Chem. Eng. Sci.*, **35**, 1980, 1341–1346.

[5] Gvozdić, B., Alméras, E., Mathai, V., Zhu, X., van Gils, D. P., Verzicco, R., Huisman, S. G., Sun, C. and Lohse, D., Experimental investigation of heat transport in homogeneous bubbly flow, *J. Fluid Mech.*, **845**, 2018, 226–244.

[6] Mercado, J. M., Gomez, D. C., van Gils, D., Sun, C. and Lohse, D., On bubble clustering and energy spectra in pseudo-turbulence, *J. Fluid. Mech.*, **650**, 2010, 287–306.

[7] Meschini, V., de Tullio, M. D., Querzoli, G. and Verzicco, R., Flow structure in healthy and pathological left ventricles with natural and prosthetic mitral valves, *J. Fluid. Mech.*, **834**, 2018, 271–307.

[8] Ng, C. S., Ooi, A., Lohse, D. and Chung, D., Vertical natural convection: application of the unifying theory of thermal convection, *J. Fluid Mech.*, **764**, 2015, 349–361.

[9] Ng, C. S., Ooi, A., Lohse, D. and Chung, D., Changes in the boundary-layer structure at the edge of the ultimate regime in vertical natural convection, *J. Fluid Mech.*, **825**, 2017, 550–572.

[10] Ngo-Cong, D., Nguyen, A. V. and Tran-Cong, T., Isotropic turbulence surpasses gravity in affecting bubble-particle collision interaction in flotation, *Minerals Engineering*, **122**, 2018, 165–175.

[11] Patterson, J. C. and Armfield, S. W., Transient features of natural convection in a cavity, *J. Fluid Mech.*, **219**, 1990, 469–497.

[12] Spandan, V., Meschini, V., Ostilla-Mónico, R., Lohse, D., Querzoli, G., de Tullio, M. D. and Verzicco, R., A parallel interaction potential approach coupled with the immersed boundary method for fully resolved simulations of deformable interfaces and membranes, *J. Comput. Phys.*, **348**, 2017, 567–590.

[13] Spandan, V., Verzicco, R. and Lohse, D., Physical mechanisms governing drag reduction in turbulent Taylor–Couette flow with finite-size deformable bubbles, *J. Fluid. Mech.*, **849**.

[14] Verzicco, R. and Orlandi, P., A finite-difference scheme for three-dimensional incompressible flows in cylindrical coordinates, *J. Comput. Phys.*, **123**, 1996, 402–414.

[15] Zwirner, L. and Shishkina, O., Confined inclined thermal convection in low-Prandtl-number fluids, *J. Fluid Mech.*, **850**, 2018, 984–1008.